RSC Advances

PAPER

View Article Online
View Journal | View Issue

Cite this: *RSC Adv.*, 2025, **15**, 2727

Enhanced response of an infrared photodetector based on hybridization between reduced graphene oxide and up-conversion microparticles†

Vuong Thanh Tuyen,[ab] Duc Anh Ngo,[ab] Le Thai Duy,[ab] Nguyen Duc Hao,[ab] Nhu Hoa Tran Thi,[ab] Vinh Quang Dang[ab] and Tran T. T. Van *[ab]

Received 7th November 2024
Accepted 15th January 2025

DOI: 10.1039/d4ra07919a

rsc.li/rsc-advances

Infrared (IR) photodetectors play an important role in many fields such as industry, medicine, security, *etc.* Achieving high response and maintaining stability in the device performance while reducing materials cost are required for the practical use of optical sensors. This study presents the development of a low-cost but high-performance IR photodetector based on a hybridization of up-conversion microparticles of $NaYF_4$:Tm,Yb (UCMPs) and reduced graphene oxide material (RGO). In this combination, UCMPs play the role of absorbing photons from 980 nm excitation light, generating electron–hole pairs, which are useful for sensing applications. Meanwhile, RGO acts as a charge collector or a charge transport layer because of its high mobility, good electro-conductivity, and large surface area. Through various characterization experiments in dark and light conditions, the analysis results confirm that our devices show sensitivity to IR light with excellent operation stability up to 30 days even stored in ambient conditions. Overall, the combination of UCMPs and RGO materials promises to increase the ability to absorb infrared light, the optical sensitivity of the photodetector.

Introduction

In the recent years, photodetectors have played an important role in optoelectronics,[1] fire safety, medical,[2] and military[3,4] applications. Particularly, optoelectronics has attracted many studies and reports on developing 'specialized' photodetectors. It is worth noting that most of them indicate the great potential of material hybridization and optimization.[5–13] Due to the working principle, the performance of the photodetectors are mainly dependent on the quality of the active materials, which absorb photons and convert them into an electrical signal. Hence, the materials are used as optoelectronic components that need to meet requirements such as high sensitivity (precision), good response (signal-to-noise differentiation), and long-term stability.

Currently, low-dimensional semiconductors such a quantum dots (QDs), up-conversion luminescent materials[14,15] and two-dimensional materials with variable band gaps (like graphene[6,16–18] and molybdenum disulfide (MoS_2)[19,20]) are receiving much research attention because of their surface properties and optical properties. Among them, graphene derivatives from graphene oxide (or reduced graphene oxide, RGO) are attracting a lot of attention from researchers, mainly because of low cost, environmental friendliness, ease of synthesis, and the band gap of these ultrathin materials (just a few layers of carbon atoms) can be tuned by controlling the number of chemical functional groups on their surface (through fabrication conditions and reducing agents).[21] However, RGO has some significant challenges, such as fast carrier recombination, low photocurrent, and weak light absorption. Thus, increasing the photodetector's capacity for reaction is a crucial challenge that many researchers are interested in.[22–26] To address this, scientists have developed hybrid materials using RGO that combine a range of inorganic and organic substances such as metal oxides, semiconductor nanoparticles, organic polymers, up-conversion luminescent micro-materials (UCMPs), and so on. Since UCMPs have outstanding chemical and physical properties, such as high photobleaching resistance, low background autofluorescence, and low toxicity, they have been of interest to many researchers for the fabrication of infrared photodetectors.

$NaYF_4$ doped with rare earths (such as Yb^{3+}, Tm^{3+}, Er^{3+}, *etc.*) operate based on the anti-Stokes shift process, in which the sequential absorption of two or more photons with longer wavelengths leads to emission of photons shorter wavelengths. Lanthanide-based UCMPs include a host material and luminescent centers that act as activators, such as erbium (Er^{3+}) and thulium (Tm^{3+}), and here, $NaYF_4$ serves as one of the most suitable host materials. Due to its low phonon energy capable of non-radiative multi-phonon inhibition. In particular,

[a]*Faculty of Materials Science and Technology, University of Science, Ho Chi Minh City, Vietnam. E-mail: tttvan@hcmus.edu.vn*

[b]*Vietnam National University, Ho Chi Minh City, Vietnam*

† Electronic supplementary information (ESI) available. See DOI: https://doi.org/10.1039/d4ra07919a

lanthanide ion-doped UCMPs are chemically stable, less harmful, have high thermal stability, and exhibit luminous efficiency. In order to enhance the IR sensing performance, this study focuses on the fabrication and characteristic properties of the hybrid infrared photodetector based on RGO and Tm,Yb-doped UCMPs ($NaYF_4$:Tm,Yb). Here, the $4f^n$ electronic configuration of the lanthanide-doped ions provides a multi-energy level system with a longer lifetime in the excited state for the generated charge carriers to transfer the RGO layer. Therefore, UCMPs act as absorbers and RGO can act as a transport layer for the charge carriers generated from UCMPs. Specifically, under the excitation light of 980 nm, UCMPs with $4f^n$ electronic configuration of lanthanide-doped ions provide a multi-energy level system with a longer lifetime in the excited state for the generated charge carriers to transfer to the RGO layer. From there, under the effect of the electric field, electrons move to one electrode, and holes move to the other electrode, creating a photocurrent. Currently, according to the most extensive survey, there has been no study combining UCMPs with RGO for use in infrared photodetectors. Therefore, this study has utilized the current signal instead of the optical signal based on UCMPs and RGO materials. Combining the above two materials promises to improve the ability to absorb light in the infrared region and the optical sensitivity of infrared sensor components. In this study, the infrared photodetector based on the combination of $NaYF_4$:Tm,Yb UCMPs and RGO shows the current–voltage characteristic result between −1 and +1 V is 7.2 $\times$ 10^5 A, and the maximum response is 1.8% under 1 V voltage and 980 nm LED illumination.

Materials & experimental

Materials

All chemicals and reagents with high grade were used. Chloroform ($CHCl_3$), stearic acid ($C_{17}H_{35}COOH$, >99.9%), sodium hydroxide (NaOH, >99.5%), sodium fluoride (NaF, >99.9%), ethanol (C_2H_5OH, >99.9%) were supplied by Merck-Germany, oleic acid ($C_{17}H_{33}COOH$, >99.0%), yttrium nitrate hexahydrate ($Y(NO_3)_3\cdot 6H_2O$, >99.9%), ytterbium nitrate pentahydrate ($Yb(NO_3)_3\cdot 5H_2O$), thulium nitrate ($Tm(NO_3)_3\cdot 5H_2O$) were provided from Sigma-Aldrich, ethanol (C_2H_5OH, >99,99% purity, Chemsol), hydrazine hydrate solution (NH_2NH_2, Sigma Aldrich), graphene oxide (GO, 99% purity, Sigma Aldrich), tetrahydrofuran (C_4H_8O, 99.5%, China).

Preparation of the materials and IR photodetectors

The hydrothermal synthesis of UCMPs was carried out in two stages: (i) the dopant preparation using rare-earth stearate (see Fig. S1a, ESI†) and (ii) the preparation of $NaYF_4$:0.5Tm,30Yb microparticles by the reported hydrothermal method[27,28] (see Fig. S1b, ESI†).

The synthesis of RGO thin films and fabrication of photodetectors are illustrated in Fig. 1. In the first stage, GO (0.5 mg mL^{-1}) in ethanol solvent was spray-coated onto a heated glass substrate and reduced with hydrazine vapor at 60 °C for 18 h. After that, the sample was cleaned with water and dried on a hot plate (at 120 °C for 2 h), forming the RGO layer.[29] Next, the silver electrode was sputtered onto the RGO channel with a thickness of 50 nm, and the sputtering parameters, including pressure, power, current, deposition rate, corresponded to 2.2 $\times$ 10^{-2} torr, 10 W, 31 mA, 329 V, and 0.71 Å s^{-1}, respectively. Besides, a mixture of isopropyl alcohol and tetrahydrofuran, with a ratio of 1 : 1, was prepared to disperse UCMPs. Then, 1 mg of UCMP was added to 1 mL of the mixture solution to obtain a good dispersion for spray-coating, which was performed and followed by drying at 100 °C for 30 min to completely evaporate the solution.

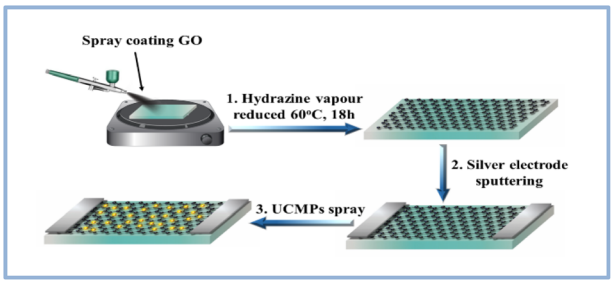

Fig. 1 Fabrication process of IR photodetector based on RGO and UCMPs.

Characterizations

The crystal structures of UCMPs, RGO and UCMPs/RGO were observed by X-ray diffraction (XRD) performed on the D8 Advance-Bruker diffractometer (operating at 40 kV, 100 mA with the Cu-Kα radiation source ($\lambda = 0.154$ nm)). Raman spectra were recorded by Raman spectrometer (Xplora One, HORIBA) with the excitation source at wavelength 532 nm, the capacity of 5 mW, and the acquisition time was adjusted to 15 s for each spectrum. The surface morphology was examined using a scanning electron microscope (FESEM, Hitachi S-4800). The optical properties of the nanorods were determined through photoluminescence spectroscopy (PL) and Diffuse Reflectance Spectroscopy (DRS). Photodetector characteristics were investigated through the current–voltage (I–V) and time-dependent current measurements (I–t), which were recorded by the system Keithley 2400. Light source (35 W LED, 980 nm, Lumixtax) is used for IR sensing under a bias of 1 V.

Results and discussions

Structural characteristics and surface morphology

In this study, X-ray diffraction (XRD) measurements were performed as shown in Fig. 2a, which shows the characteristic diffraction peaks of RGO and hybrid UCMPs/RGO samples. The pattern of the UCMPs/RGO hybrid sample shows diffraction peaks consistent with the hexagonal structure of UCMPs, which are located at $2\theta = 17.25°$, 30.03°, 30.92°, 34.80°, 39.75°, 43.59°, 46.57°, 52.27° and 53.23° corresponding to (100), (110), (101), (200), (111), (201), (210), (102) and (300) planes, respectively; here, the crystallization of UCMPs is referenced to the JCPDS card number 16-0334 (see Fig. S2, ESI†).[30–33] In addition, that pattern displays the typical characteristic diffraction peak of

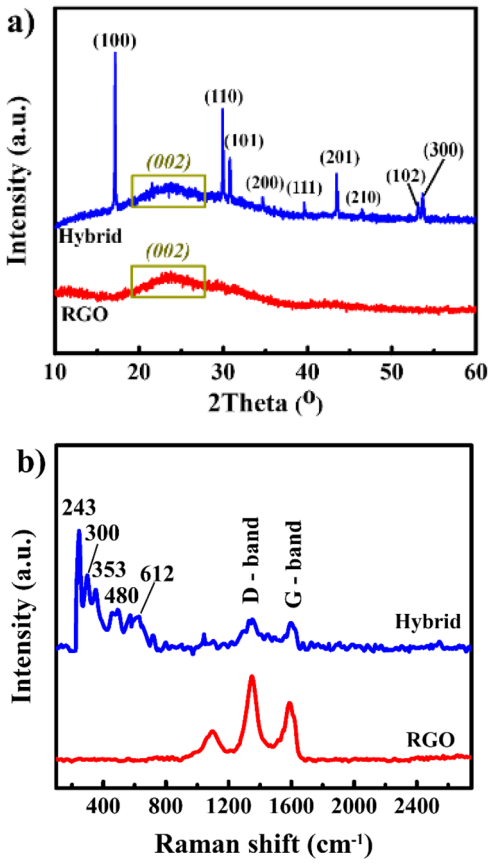

Fig. 2 (a) XRD patterns and (b) Raman spectra of RGO and hybrid UCMPs/RGO.

RGO at 24.4°.[34–36] The XRD pattern shows no other peaks, indicating the absence of contamination chemicals in our samples.

To confirm the formation of RGO, Raman spectroscopy was carried out, as shown in Fig. 2b. The Raman spectrum of the UCMPs/RGO hybrid sample has five prominent peaks with high intensities at wavenumbers of 245 cm^{-1}, 298 cm^{-1}, 350 cm^{-1}, 490 cm^{-1}, and 600 cm^{-1}, indicating the hexagonal phase of UCMPs (Fig. S3, ESI†). Furthermore, this Raman spectrum displays two characteristic signals of RGO: the disorder band arising from the graphite edges (D band) at around 1385 cm^{-1} and the in-phase vibration of the graphite lattice (G band) at wavenumber 1575 cm^{-1}.[34,35,37,38] Consequently, the Raman results agree with that of XRD, and they both confirm the successful formation of the UCMPs/RGO hybrid sample.

To characterize the active channel's morphology, field emission scanning electron microscopy (FESEM) and transmission electron microscopy (TEM) measurements were performed. Fig. 3a and b show FESEM images of RGO and UCMPs, respectively. The FESEM images show clear contrast between areas with thick and thin RGO layers. The UCMPs present a branched structure with a particle size of >200–1000 nm. Additionally, the TEM images of the UCMPs/RGO hybrid sample in Fig. 3c and d show that the UCMPs are evenly distributed on RGO, indicating their uniform distribution.

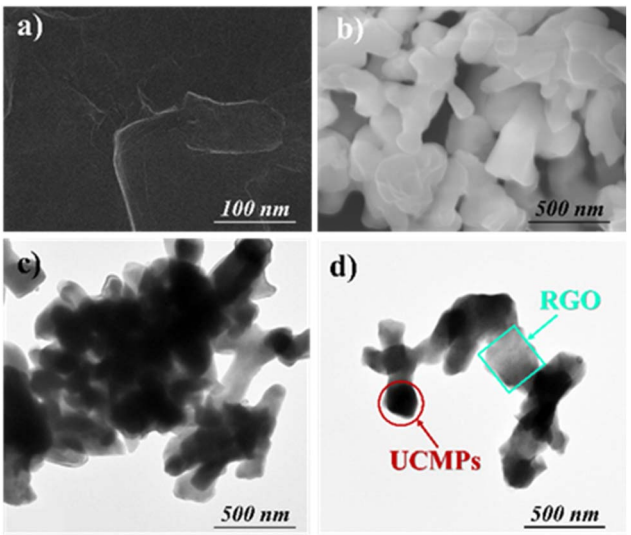

Fig. 3 FESEM images of (a) RGO and (b) UCMPs; (c) and (d) TEM image of the UCMPs/RGO hybrid.

Optical properties

To prove that charge transfer occurs between UCMPs and RGO, this study measured the photoluminescence spectroscopy (PL) of UCMPs and hybrid UCMPs/RGO samples (Fig. 4). When UCMPs are excited with the 980 nm IR light, their PL spectrum presents various emission peaks at wavelengths of 365, 375, 451, 475, 646, 693, and 790 nm that correspond to the transition levels $^3P_1 \rightarrow {}^3H_5$, $^1D_2 \rightarrow {}^3H_6$, $^1D_2 \rightarrow {}^3F_4$, $^1G_4 \rightarrow {}^3H_6$, $^1G_4 \rightarrow {}^3F_4$, $^3F_3 \rightarrow {}^3H_6$, and $^3H_4 \rightarrow {}^3H_6$, respectively.[39–42] Here, the 4f orbital is shielded by the 5s and 5p shells, which results in intense absorption and emission. Along with emission peaks at 365, 375, 451, 475, 646, 693, and 790 nm on the PL spectra of the hybrid UCMPs/RGO sample exhibits lower emission intensity than that of UCMPs. The lack of hole can promote non-radiative

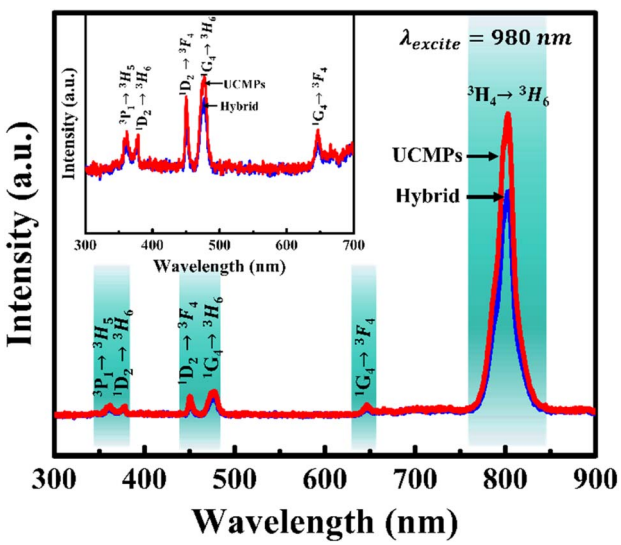

Fig. 4 PL spectra of UCMPs and hybrid UCMPs/RGO.

recombination processes leading to an increase of the rate of energy loss as heat. As a result, the luminescence efficiency decreases.

Characteristic properties of IR photodetectors

Fig. 5a shows the schematic structure of the IR sensing device based on UCMP/RGO hybrid material. As mentioned, the RGO component acts as the transport layer, and the UCMPs act as the photo absorber and the charge carrier donator to RGO *via* their energy-level alignment. The characteristics of the properties of photodetectors are tested under the voltage range of 0 to +1 V and the 980 nm light excitation, as shown in Fig. 5b and c. Here, the figure reveals (i) an excellent ohmic contact between RGO and Ag electrodes that could provide the linear *I*–*V* curve (with low noise) and (ii) a clear increase and a recovery of the device current when the IR light was on and off, respectively.

The response characteristics of our photodetectors based on RGO and hybrid UCMPs/RGO are shown in Fig. 6 and 7, respectively. To control the response of the photodetector, the lighting conditions are guaranteed to not change, and a light chopper is used to control the light exposure. The response capacity of the photodetector is calculated according to eqn (1), in which I_{dark} is recorded without lighting, and I_{light} is recorded at the end of the illumination period.[43]

$$\text{Response} = [(I_{light} - I_{dark})/I_{dark}] \times 100\% \quad (1)$$

For devices based on RGO and hybrid UCMPs/RGO with the same conditions (illumination time of 50 s, voltage of 1 V, and 980 nm-light illumination). For the same 50 s illumination period, Fig. 6a displays the hybrid UCMPs/RGO and the RGO device reaching the response maximum 1.8% and 0.4%, respectively. Moreover, the response percentage of the hybrid UCMPs/RGO photodetector is higher than the RGO photodetector (see Fig. 6b). This difference shows that the absorption capacity of UCMPs decreases electron–hole pair recombination, increasing device response by as much as 2.4% and 0.02% s^{-1}.[44,45]

To compare the response of the RGO and UCMPs/RGO hybrid-based photodetectors, the devices were studied under different illumination cycles and the identical illumination conditions of wavelength 980 nm and a 1 V voltage. Fig. 7a shows the response characteristics of RGO based photodetector under a 980 nm wavelength with illumination times of 20 s, 30 s, 40 s, 50 s, 60 s, 70 s, 80 s, and 90 s. The response of RGO in range of 0.23% and 0.63% can be explained that RGO has a very small bandgap, enabling it to respond under 980 nm wavelength light.[46–48] However, RGO has high mobility, which leads to a relatively high recombination rate. Fig. 7b presents the response of UCMPs/RGO hybrid devices with increasing illumination time under 980 nm excitation. For the UCMPs/RGO hybrid device, when increasing different illumination times in 8 cycles from 20 s, 30 s, 40 s, 50 s, 60 s, 70 s, 80 s, and 90 s. The response percentage of the hybrid device increased linearly with the illumination time from 1.25% to 2.4%. This shows that the photo responsiveness of the hybrid device is higher than that of the RGO device. Fig. 7c and d shows the response of the UCMPs/RGO hybrid device with illumination times of 30 s and 70 s for multiple cycles under the same excitation wavelength of

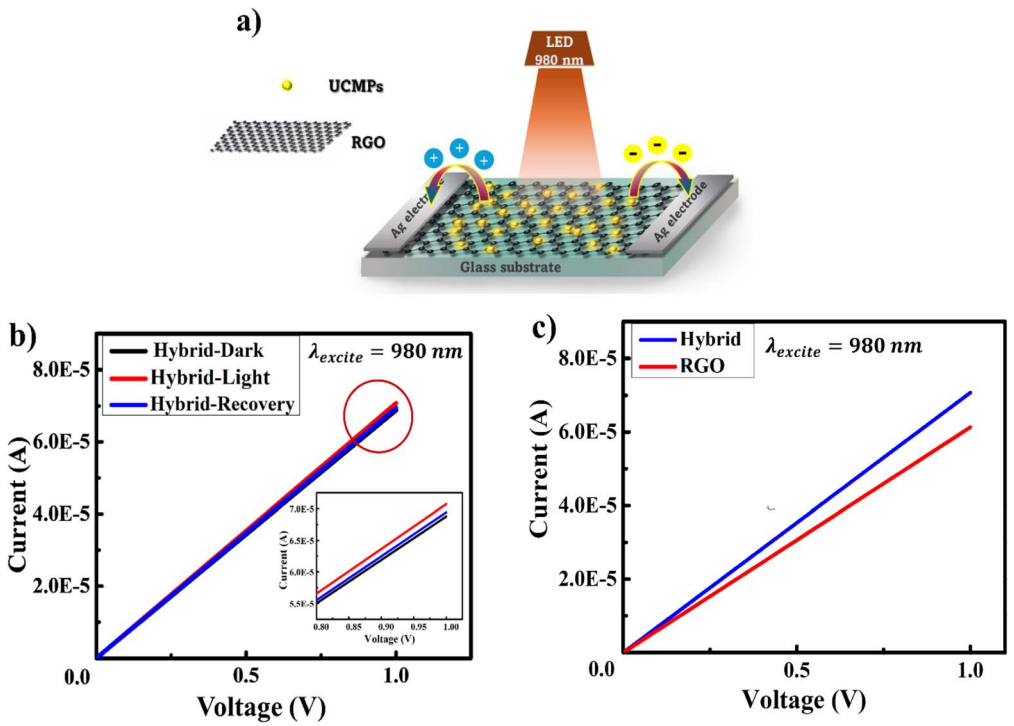

Fig. 5 (a) Schematic structure of the IR photodetector based on UCMPs/RGO; (b) *I*–*V* characteristics of hybrid UCMPs/RGO in dark and light conditions; (c) comparing the *I*–*V* curves of RGO and hybrid UCMPs/RGO under 980 nm LED illumination.

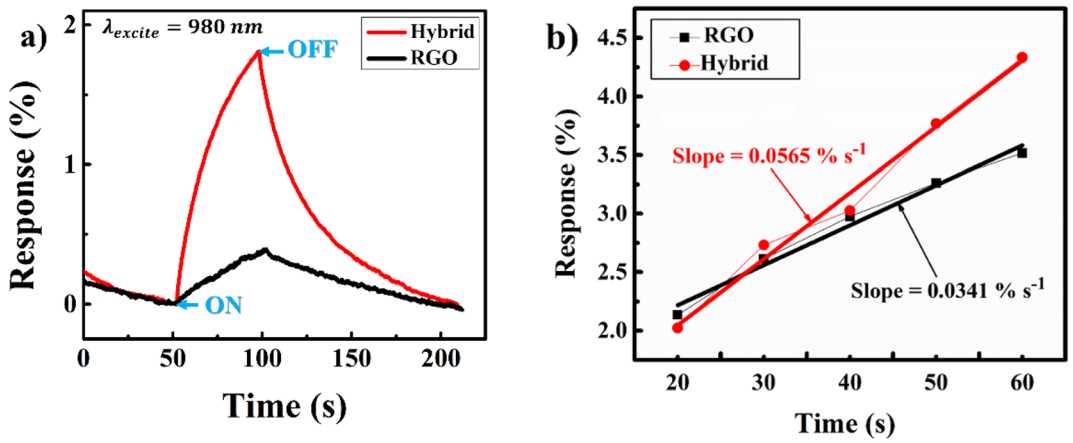

Fig. 6 (a) Response of hybrid UCMPs/rGO and (b) sensitivity or response speed (*i.e.*, the linear fitting slope) of RGO and hybrid UCMPs/rGO under 980 nm-light illumination.

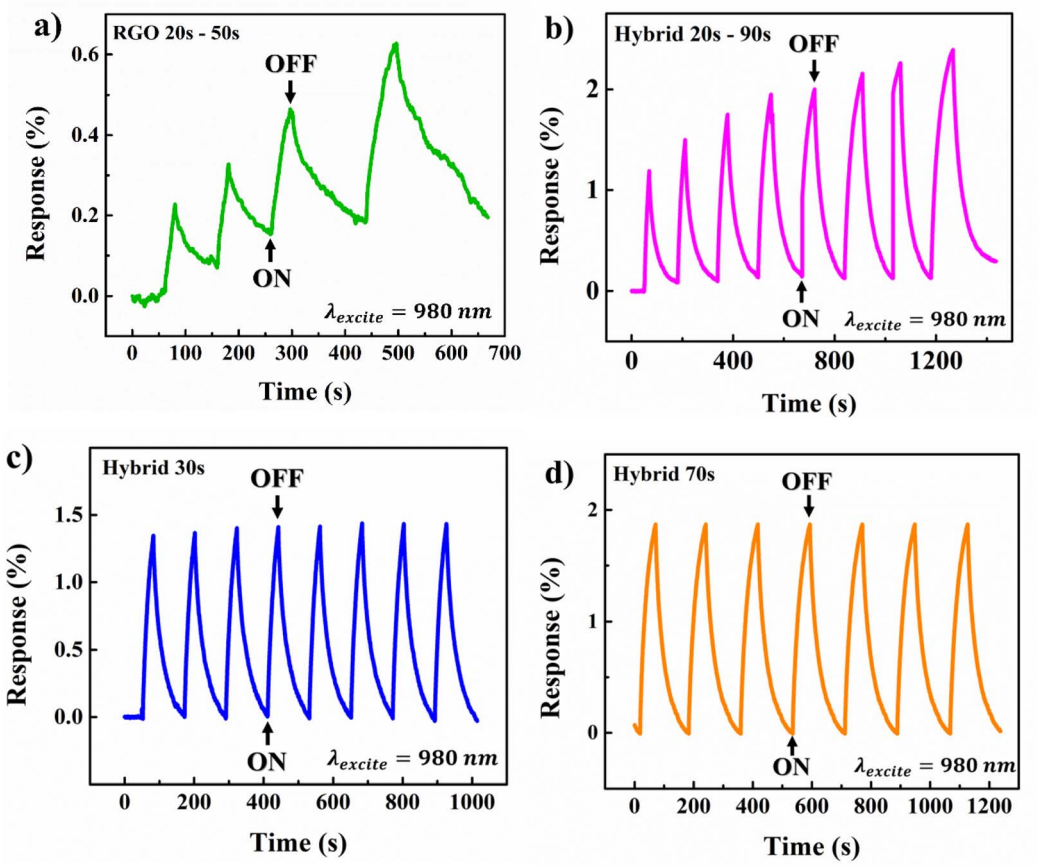

Fig. 7 (a) and (b) Response of RGO and UCMPs/RGO with various exposure time, respectively; (c) and (d) cyclic sensing tests of UCMPs/RGO with 30 and 70 s of exposure, respectively.

980 nm. This shows that the response time and return time after the same illumination time and multiple consecutive cycles remain unchanged. Therefore, this illustrates that the photodetector has a very stable response.

In addition, this study also investigated the response of the photodetector after 30 days of preparation. The time-resolved photocurrent of the UCMPs/RGO hybrid after 30 days of fabrication is presented in Fig. 8a. As shown here, the response current of the latter device reached a value of 0.14% when illuminated by an excitation of 980 nm for 50 s. Due to the oxidation of the surface of the photosensitive material in ambient conditions, which hinders the movement of

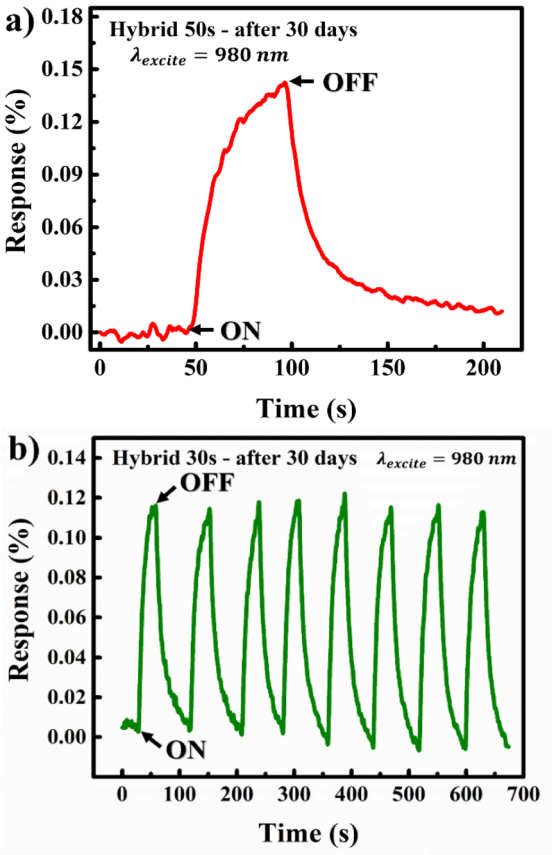

Fig. 8 Response of (a) hybrid UCMPs/RGO; (b) hybrid UCMPs/RGO in the same cycles after 30 days manufactured under a 980 nm illumination.

photogenerated electrons or increases the recombination of electron–hole pairs, the number of photons converted into electrical signals is reduced, causing the signal to be weak, thereby leading to a decrease in the response of the sensor. Although the response decreased significantly, the high stability and good reproducibility of the sensor are shown in Fig. 8b. This can confirm that the fabrication process and design of the photodetector have achieved consistency after 30 days of fabrication.

Furthermore, the two important parameters, responsivity (A W^{-1}) and detectivity (Jones), have been calculated using the eqn (2) and (3):

$$\text{Responsivity } (R) = \frac{I_{\text{light}} - I_{\text{dark}}}{PA} \quad (2)$$

When I_{dark} is the current measured in the dark condition, I_{light} is the current after 50 s turning on the light, P is the incident light intensity and A is the effective device area (0.3 cm^2) in the given order.

$$\text{Detectivity } (D) = R\left(\frac{A}{2eI_{\text{dark}}}\right)^{1/2} \quad (3)$$

From these formulas, we calculated the responsivity and detectivity to be 162 × 10^{-3} A W^{-1} and 244 × 10^{-3} Jones, respectively.

Besides, the response time of the photodetector is defined as the time to reach 90% of its maximum photocurrent, while the recovery time is defined as the duration for the photocurrent to return to 10% of its highest value (Fig. S4, ESI†).[49] Therefore, the response time achieved is 55 s and the recovery time is 175 s under 980 nm excitation light.

In this study, a comparison of the sensor's response under wavelengths shorter than 980 nm was conducted. This is shown in Fig. S5 (ESI†). It shows that the photodetector's response at 980 nm is 0.91%, with no signal detected at 480 nm and 510 nm, indicating that the sensor does not effectively respond to these shorter wavelengths. Because the 980 nm wavelength has energy (1.26 eV) that matches the energy levels of Yb^{3+} and Tm^{3+}, it creates a special resonance with the 980 nm wavelength, while wavelengths of 410 nm and 580 nm are not compatible. This allows the upconversion process to occur in UCMPs, where the optical sensor based on the UCMPs/RGO hybrid operates according to the mechanism discussed in the following section.

The results of the photodetector and its comparison with some other reported devices are presented in Table 1. Although the performance of this hybrid UCMPs/RGO device is not the best, it still outperforms several other devices.

Optical sensing mechanism

The combination of reduced graphene oxide (RGO) transfer layer, and upconverted $NaYF_4$:Tm,Yb materials (UCMPs) results in a highly sensitive, stable photodetector. When UCMPs are excited by wavelength of 980 nm, the absorption of the two- or

Table 1 Comparison of responsivities of other photodetectors

Materials structure	Wavelength (nm)	Responsivity (A W^{-1})	Ref.
Graphene/GaAs	980	0.00597	50
UCNPs/MoS_2	980	1254	51
UCNPs on CdS	980	2.15 × 10^2	52
SiO_2@UCNPs on CdS	980	0.118	
Graphene/HfO_2/a-MoS_2	From 473 to 2712	5.36	53
UCNPs/graphene/SiO_2/Si	661	84.52	54
Graphene/Al_2O_3	880	8 × 10^{-3}	55
Metal–graphene–metal	1550	6.1 × 10^{-3}	56
UCMPs/RGO	980	162 × 10^{-3}	This work

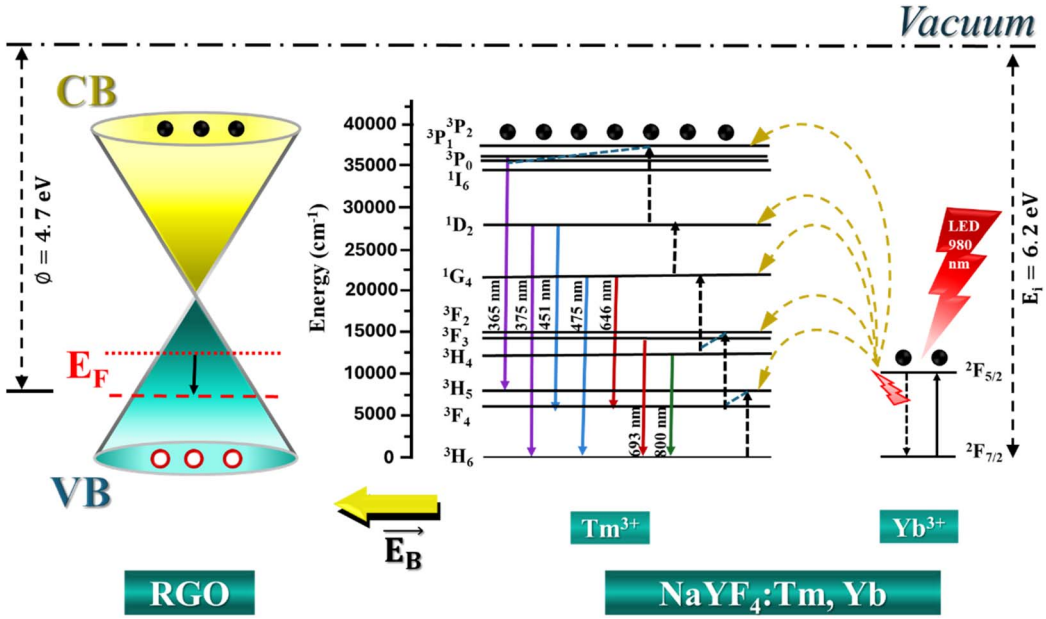

Fig. 9 Charge-transfer mechanism of hybrid UCMPs/RGO.

three-photon phenomenon in UCMPs leads to the generation of an increasing number of electrons in excited states. The unique characteristic of discrete energy levels in rare-earth-doped up-conversion materials is highly useful for achieving a highly sensitive photodetector. However, UCMPs have no direct charge driven pathways between those particles; indeed, they need RGO as a charge transport layer to contribute charges to the device channel. Therefore, the RGO film has a high electrical mobility, which acts as a bridge for charge transfer between the UCMPs and the silver electrodes. Under the dark condition of 1 V (applied to the silver electrode), holes move toward the negative electrode, generating an electric current. The charge transfer mechanism of the infrared optical sensor based on the hybrid material UCMPs and RGO is shown in Fig. 9. When the active material is excited by 980 nm light, it generates a positive current due to electrons remaining in metastable states, leading to a reduction in the Fermi level of the graphene layer. This explanation is supported by the photoluminescence spectra of UCMPs and the hybrid UCMPs/RGO in Fig. 4.

Conclusions

In summary, we successfully combined RGO and UCMPs for IR light detection. In this study, the hybrid photodetector showed a high photocurrent, high efficiency, and good stability. The mechanism behind that was explored, and it originates from the charge transfer between UCMPs and RGO under light exposure, which raised the electron-richness in the active channel. Furthermore, due to the high chemical stability of UCMPs, the RGO layer got protection, and that allows the hybrid channel to operate more efficiently (faster response and recovery along with a long lifetime). This was evidenced by the investigation of the stability of the material and the long-term performance of the device. Here, the consistent response over time highlights the potential of UCMPs/RGO hybrid materials, confirming the feasibility of RGO and UCMPs materials for highly reliable and efficient optical sensors, leading to further advances in optoelectronics and sensing technologies.

Data availability

The data supporting this article have been included as part of the ESI.†

Author contributions

Vuong Thanh Tuyen: synthesis, formal analysis, investigation, writing – original draft; Duc Anh Ngo: synthesis, measurement; Le Thai Duy: review & editing; Nguyen Duc Hao: synthesis; Nhu Hoa Tran Thi: measurement, analysis; Vinh Quang Dang: formal analysis, investigation, writing – review & editing; Tran T. T. Van: conceptualization, investigation, writing – review & editing, supervision.

Conflicts of interest

There are no conflicts to declare.

Acknowledgements

This research is funded by University of Science, VNU-HCM under grant number T2024-61.

References

1 X. Cai, S. Wang and L. M. Peng, *Recent progress of photodetector based on carbon nanotube film and application*

in optoelectronic integration, Tsinghua University Press, 2023, DOI: 10.26599/NRE.2023.9120058.

2 G. Llosá, Recent developments in photodetection for medical applications, *Nucl. Instrum. Methods Phys. Res., Sect. A*, 2015, **787**, 353–357, DOI: 10.1016/j.nima.2015.01.071.

3 H. Chen, K. Liu, L. Hu, A. A. Al-Ghamdi and X. Fang, *New concept ultraviolet photodetectors*, Elsevier B.V., 2015, DOI: 10.1016/j.mattod.2015.06.001.

4 S. K. Behura, C. Wang, Y. Wen and V. Berry, Graphene–semiconductor heterojunction sheds light on emerging photovoltaics, *Nat. Photonics*, 2019, **13**(5), 312–318, DOI: 10.1038/s41566-019-0391-9.

5 C. H. Yeh, *et al.*, Ultrafast Monolayer In/Gr-WS_2-Gr Hybrid Photodetectors with High Gain, *ACS Nano*, 2019, **13**(3), 3269–3279, DOI: 10.1021/acsnano.8b09032.

6 Y. Wang, V. X. Ho, P. Pradhan, M. P. Cooney and N. Q. Vinh, Interfacial Photogating Effect for Hybrid Graphene-Based Photodetectors, *ACS Appl. Nano Mater.*, 2021, **4**(8), 8539–8545, DOI: 10.1021/acsanm.1c01931.

7 M. Zhao, *et al.*, Interface Engineering-Assisted 3D-Graphene/Germanium Heterojunction for High-Performance Photodetectors, *ACS Appl. Mater. Interfaces*, 2020, **12**(13), 15606–15614, DOI: 10.1021/acsami.0c02485.

8 S. Shafique, *et al.*, Improving the performance of V_2O_5/rGO hybrid nanocomposites for photodetector applications, *Sens. Actuators, A*, 2021, **332**, 113073, DOI: 10.1016/j.sna.2021.113073.

9 J. Huang, *et al.*, High-performance graphene/n-Si hybrid photodetector toward self-driven optical communications, *Appl. Phys. Lett.*, 2021, **119**(26), 263506, DOI: 10.1063/5.0064366.

10 K. Zhang, *et al.*, Hybrid structure of PbS QDs and vertically few-layer MoS_2 nanosheets array for broadband photodetector, *Nanotechnology*, 2021, **32**(14), 145602, DOI: 10.1088/1361-6528/abd57f.

11 S. N. S. Yadav, *et al.*, Enhanced Photoresponsivity of Perovskite QDs/Graphene Hybrid Gate-Free Photodetector by Morphologically Controlled Plasmonic Au Nanocrystals, *Adv. Opt. Mater.*, 2023, **11**(15), 2300131, DOI: 10.1002/adom.202300131.

12 Y. Ji, D. Zhou, N. Wang, N. Ding, W. Xu and H. Song, Flexible double narrowband near-infrared photodetector based on PMMA/core–shell upconversion nanoparticle composites, *J. Rare Earths*, 2022, **40**(2), 211–217, DOI: 10.1016/j.jre.2020.12.001.

13 M. Irfan, H. Mustafa, A. Sattar, A. Usman, M. Sajid and S. Qin, Investigating the Impact of Upconversion Nanoparticles on the Photodetection Characteristics of Graphene/MoS_2 Heterostructure-Based Photodetectors, available: https://ssrn.com/abstract=4555617.

14 H. Zhang, *et al.*, Near-Infrared Light-Sensitive Hole-Transport-Layer Free Perovskite Solar Cells and Photodetectors with Hexagonal $NaYF_4$:Yb^{3+},Tm^{3+}@SiO_2 Upconversion Nanoprism-Modified TiO_2 Scaffold, *ACS Sustain. Chem. Eng.*, 2019, **7**(9), 8236–8244, DOI: 10.1021/acssuschemeng.8b06606.

15 H. Zhang, *et al.*, Near-Infrared Light-Sensitive Hole-Transport-Layer Free Perovskite Solar Cells and Photodetectors with Hexagonal $NaYF_4$:Yb^{3+},Tm^{3+}@SiO_2 Upconversion Nanoprism-Modified TiO_2 Scaffold, *ACS Sustain. Chem. Eng.*, 2019, **7**(9), 8236–8244, DOI: 10.1021/acssuschemeng.8b06606.

16 Y. Zhang, *et al.*, Graphdiyne-Based Flexible Photodetectors with High Responsivity and Detectivity, *Adv. Mater.*, 2020, **32**(23), 2001082, DOI: 10.1002/adma.202001082.

17 F. H. L. Koppens, T. Mueller, P. Avouris, A. C. Ferrari, M. S. Vitiello and M. Polini, *Photodetectors based on graphene, other two-dimensional materials and hybrid systems*, Nature Publishing Group, 2014, DOI: 10.1038/nnano.2014.215.

18 J. Li, *et al.*, Metamaterial grating-integrated graphene photodetector with broadband high responsivity, *Appl. Surf. Sci.*, 2019, **473**, 633–640, DOI: 10.1016/j.apsusc.2018.12.194.

19 C. Gao, *et al.*, Templated-Construction of Hollow MoS_2 Architectures with Improved Photoresponses, *Adv. Sci.*, 2020, **7**(22), 2002444, DOI: 10.1002/advs.202002444.

20 B. Mehrdel, A. Nikbakht, A. A. Aziz, M. S. Jameel, M. A. Dheyab and P. M. Khaniabadi, *Upconversion lanthanide nanomaterials: basics introduction, synthesis approaches, mechanism and application in photodetector and photovoltaic devices*, IOP Publishing Ltd, 2022, DOI: 10.1088/1361-6528/ac37e3.

21 C. Bonavolontà, *et al.*, Reduced graphene oxide on silicon-based structure as novel broadband photodetector, *Sci. Rep.*, 2021, **11**(1), 13015, DOI: 10.1038/s41598-021-92518-z.

22 Y. Sandali and M. Sulaman, Synthesis and characterization of WO_3/BiS_2/rGO composites for enhanced optoelectronic performance in photodetector applications, *Mater. Sci. Eng., B*, 2024, **303**, 117316, DOI: 10.1016/j.mseb.2024.117316.

23 M. Li, *et al.*, Improving performance of hybrid perovskite/graphene-based photodetector via hot carriers injection, *J. Alloys Compd.*, 2022, **895**, 162496, DOI: 10.1016/j.jallcom.2021.162496.

24 P. K. Inaniya, R. K. Maddila and R. Mehra, Development of rGO based photodetector for visible light detection applications, *Mater. Today: Proc.*, 2023, 1–4, DOI: 10.1016/j.matpr.2023.04.289.

25 A. Gupta, *et al.*, Record-High Responsivity and High Detectivity Broadband Photodetectors Based on Upconversion/Gold/Prussian-Blue Nanocomposite, *Adv. Funct. Mater.*, 2022, **32**(44), 2206496, DOI: 10.1002/adfm.202206496.

26 Y. Zeng, X. Hu, S. Cheng, X. Wu, S. Zhan and Y. Liu, High performance infrared photodetectors based on CdS film activated by lanthanide-doped upconverting nanoparticles, *Ceram. Int.*, 2024, **50**(8), 13960–13966, DOI: 10.1016/j.ceramint.2024.01.313.

27 V. T. Tuyen, *et al.*, Controllable structural and optical properties of $NaYF_4$:Tm, Yb microparticles by Yb^{3+} doping for anti-counterfeiting, *RSC Adv.*, 2023, **13**(28), 19317–19324, DOI: 10.1039/d3ra02841k.

28 T. T. Vuong, B. T. Nguyen, H. Van Le, T. M. D. Cao and T. T. Van Tran, Investigating the effect of synthesis parameters on the structure and upconversion luminescent properties of $NaYF_4$:Tm,Yb for anticounterfeiting printing ink, *Science and Technology Development Journal*, 2024, 19317, DOI: 10.32508/stdj.v27i1.4223.

29 D. A. Ngo, *et al.*, A study on a broadband photodetector based on hybrid 2D copper oxide/reduced graphene oxide, *Nanoscale Adv.*, 2024, **6**(5), 1460–1466, DOI: 10.1039/d3na00796k.

30 C. Q. Yang, *et al.*, Paramagnetism and improved upconversion luminescence properties of $NaYF_4$:Yb,Er/$NaGdF_4$ nanocomposites synthesized by a boiling water seed-mediated route, *Frontiers of Materials Science*, 2016, **10**(1), 38–44, DOI: 10.1007/s11706-016-0318-z.

31 X. Xue, *et al.*, Laser power density dependent energy transfer between Tm^{3+} and Tb^{3+}: tunable upconversion emissions in $NaYF_4$:Tm^{3+},Tb^{3+},Yb^{3+} microcrystals, *Opt. Express*, 2016, **24**(23), 26307, DOI: 10.1364/oe.24.026307.

32 M. Ding, *et al.*, Controlled synthesis of β-$NaYF_4$:Yb^{3+}/Er^{3+} microstructures with morphology- and size-dependent upconversion luminescence, *Ceram. Int.*, 2015, **41**(6), 7411–7420, DOI: 10.1016/j.ceramint.2015.02.054.

33 H. Guan, Y. Feng, W. Zhang, W. Wang and Y. Hu, Room-temperature facile synthesis of hexagonal $NaYF_4$ and $NaYF_4$: Yb, Er powder without any organic additives and its upconversion fluorescence properties, *Adv. Powder Technol.*, 2022, **33**(1), 2206496, DOI: 10.1016/j.apt.2021.11.033.

34 X. Qiao, S. Liao, C. You and R. Chen, Phosphorus and nitrogen dual doped and simultaneously reduced graphene oxide with high surface area as efficient metal-free electrocatalyst for oxygen reduction, *Catalysts*, 2015, **5**(2), 981–991, DOI: 10.3390/catal5020981.

35 G. Yasin, *et al.*, Exploring the Nickel–Graphene Nanocomposite Coatings for Superior Corrosion Resistance: Manipulating the Effect of Deposition Current Density on Its Morphology, Mechanical Properties, and Erosion-Corrosion Performance, *Adv. Eng. Mater.*, 2018, **20**(7), 1701166, DOI: 10.1002/adem.201701166.

36 M. R. D'Oliveira, J. Rabelo, A. G. Veiga, C. A. Chagas and M. Schmal, In Situ DRIFTS Investigation of Ethylene Oxidation on Ag and Ag/Cu on Reduced Graphene Oxide, *Catal. Lett.*, 2020, **150**(10), 3036–3048, DOI: 10.1007/s10562-020-03208-w.

37 W. E. Ghann, *et al.*, Synthesis and characterization of reduced graphene oxide and their application in dye-sensitized solar cells, *ChemEngineering*, 2019, **3**(1), 1–13, DOI: 10.3390/chemengineering3010007.

38 Y. S. Chang, F. K. Chen, D. C. Tsai, B. H. Kuo and F. S. Shieu, N-doped reduced graphene oxide for room-temperature NO gas sensors, *Sci. Rep.*, 2021, **11**(1), 20719, DOI: 10.1038/s41598-021-99883-9.

39 S. Ullah, C. Hazra, E. P. Ferreira-Neto, T. C. Silva, U. P. Rodrigues-Filho and S. J. L. Ribeiro, Microwave-assisted synthesis of $NaYF_4$:Yb^{3+}/Tm^{3+} upconversion particles with tailored morphology and phase for the design of UV/NIR-active $NaYF_4$:Yb^{3+}/Tm^{3+}@TiO_2 core@shell photocatalysts, *CrystEngComm*, 2017, **19**(25), 3465–3475, DOI: 10.1039/c7ce00809k.

40 S. Xu, *et al.*, $NaYF_4$:Yb,Tm nanocrystals and TiO_2 inverse opal composite films: a novel device for upconversion enhancement and solid-based sensing of avidin, *Nanoscale*, 2014, **6**(11), 5859–5870, DOI: 10.1039/c4nr00224e.

41 Z. Yi, G. Ren, L. Rao, H. Wang, H. Liu and S. Zeng, Tunable multicolor upconversion luminescence and paramagnetic property of the lanthanide doped fluorescent/magnetic bi-function $NaYbF_4$ microtubes, *J. Alloys Compd.*, 2014, **589**, 502–506, DOI: 10.1016/j.jallcom.2013.12.036.

42 Y. He, *et al.*, Perovskite quantum dots modulating upconversion nanomaterials for cancer early detections, *Cancer Nanotechnol.*, 2023, **14**(1), 52, DOI: 10.1186/s12645-023-00206-6.

43 A. A. Ahmed, M. Devarajan and N. Afzal, Fabrication and characterization of high performance MSM UV photodetector based on NiO film, *Sens. Actuators, A*, 2017, **262**, 78–86, DOI: 10.1016/j.sna.2017.05.028.

44 S. Shafique, *et al.*, Improving the performance of V_2O_5/rGO hybrid nanocomposites for photodetector applications, *Sens. Actuators, A*, 2021, **332**, 113073, DOI: 10.1016/j.sna.2021.113073.

45 M. Azarang, A. Shuhaimi, R. Yousefi and M. Sookhakian, Effects of graphene oxide concentration on optical properties of ZnO/RGO nanocomposites and their application to photocurrent generation, *J. Appl. Phys.*, 2014, **116**(8), 084307, DOI: 10.1063/1.4894141.

46 N. Sharma, M. Arif, S. Monga, M. Shkir, Y. K. Mishra and A. Singh, Investigation of bandgap alteration in graphene oxide with different reduction routes, *Appl. Surf. Sci.*, 2020, **513**, 1–13, DOI: 10.1016/j.apsusc.2020.145396.

47 H. Huang, Z. Li, J. She and W. Wang, Oxygen density dependent band gap of reduced graphene oxide, *J. Appl. Phys.*, 2012, **111**(5), 054317, DOI: 10.1063/1.3694665.

48 Abid, P. Sehrawat, S. S. Islam, P. Mishra and S. Ahmad, Reduced graphene oxide (rGO) based wideband optical sensor and the role of temperature, defect states and quantum efficiency, *Sci. Rep.*, 2018, **8**(1), 48, DOI: 10.1038/s41598-018-21686-2.

49 S. Safa, S. Mokhtari, A. Khayatian and R. Azimirad, Improving ultraviolet photodetection of ZnO nanorods by Cr doped ZnO encapsulation process, *Opt. Commun.*, 2018, **413**, 131–135, DOI: 10.1016/j.optcom.2017.12.038.

50 J. Wu, *et al.*, Enhanced performance of a graphene/GaAs self-driven near-infrared photodetector with upconversion nanoparticles, *Nanoscale*, 2018, **10**(17), 8023–8030, DOI: 10.1039/c8nr00594j.

51 S. Ghosh, W. C. Chiang, M. Y. Fakhri, C. T. Wu, R. S. Chen and S. Chattopadhyay, Ultrasensitive broadband photodetector using electrostatically conjugated MoS_2-upconversion nanoparticle nanocomposite, *Nano Energy*, 2020, **67**, 104258, DOI: 10.1016/j.nanoen.2019.104258.

52 Y. Zeng, X. Hu, S. Cheng, X. Wu, S. Zhan and Y. Liu, High performance infrared photodetectors based on CdS film

activated by lanthanide-doped upconverting nanoparticles, *Ceram. Int.*, 2024, **50**(8), 13960–13966, DOI: **10.1016/j.ceramint.2024.01.313**.

53 Z. Huang, *et al.*, Interfacial Gated Graphene Photodetector with Broadband Response, *ACS Appl. Mater. Interfaces*, 2021, **13**(19), 22796–22805, DOI: **10.1021/acsami.1c02738**.

54 Z. Chen, *et al.*, High Responsivity, Broadband, and Fast Graphene/Silicon Photodetector in Photoconductor Mode, *Adv. Opt. Mater.*, 2015, **3**(9), 1207–1214, DOI: **10.1002/adom.201500127**.

55 C. G. Kang, *et al.*, Highly sensitive wide bandwidth photodetectors using chemical vapor deposited graphene, *Appl. Phys. Lett.*, 2014, **104**(16), 161902, DOI: **10.1063/1.4872267**.

56 T. Mueller, F. Xia and P. Avouris, Graphene photodetectors for high-speed optical communications, *Nat. Photonics*, 2010, **4**(5), 297–301, DOI: **10.1038/nphoton.2010.40**.